J. Neural Eng. **9** (2012) 036006 (16pp) doi:10.1088/1741-2560/9/3/036006

Reconstruction of movement-related intracortical activity from micro-electrocorticogram array signals in monkey primary motor cortex

Hidenori Watanabe[1,2,8], **Masa-aki Sato**[2], **Takafumi Suzuki**[3], **Atsushi Nambu**[4,5], **Yukio Nishimura**[1,5,6], **Mitsuo Kawato**[7] **and Tadashi Isa**[1,5]

[1] Division of Behavioral Development, Department of Developmental Physiology, National Institute for Physiological Sciences, Aichi, Japan
[2] Neural Information Analysis Laboratories, Advanced Telecommunications Research Institute International, Kyoto, Japan
[3] Graduate School of Information Science and Technology, The University of Tokyo, Tokyo, Japan
[4] Division of System Neurophysiology, Department of Integrative Physiology, National Institute for Physiological Sciences, Aichi, Japan
[5] The Graduate University for Advanced Studies, Kanagawa, Japan
[6] Precursory Research for Embryonic Science and Technology, Japan Science and Technology Agency, Tokyo, Japan
[7] Computational Neuroscience Laboratories, Advanced Telecommunications Research Institute International, Kyoto, Japan

E-mail: watanabe@nips.ac.jp

Received 5 December 2011
Accepted for publication 12 April 2012
Published 9 May 2012
Online at stacks.iop.org/JNE/9/036006

Abstract
Subdural electrode arrays provide stable, less invasive electrocorticogram (ECoG) recordings of neural signals than multichannel needle electrodes. Accurate reconstruction of intracortical local field potentials (LFPs) from ECoG signals would provide a critical step for the development of a less invasive, high-performance brain–machine interface; however, neural signals from individual ECoG channels are generally coarse and have limitations in estimating deep layer LFPs. Here, we developed a high-density, 32-channel, micro-ECoG array and applied a sparse linear regression algorithm to reconstruct the LFPs at various depths of primary motor cortex (M1) in a monkey performing a reach-and-grasp task. At 0.2 mm beneath the cortical surface, the real and estimated LFPs were significantly correlated (correlation coefficient (r); 0.66 $\pm$ 0.11), and the r at 3.2 mm was still as high as 0.55 $\pm$ 0.04. A time-frequency analysis of the reconstructed LFP showed clear transition between resting and movements by the monkey. These methods would be a powerful tool with wide-ranging applicability in neuroscience studies.

(Some figures may appear in colour only in the online journal)

Introduction

Multichannel spike signals recorded from the motor cortex provide rich information about kinematic parameters of movements, such as the trajectory and velocity of the hand and arm, which are useful in the control of brain–machine interfaces (BMIs) (Georgopoulos *et al* 1982, Moran and Schwartz 1999, Hochberg *et al* 2006, Velliste *et al* 2008). Although the spike signals carry rich information about neural processing, recordings from multi-neuron spike discharges

[8] Author to whom any correspondence should be addressed.

with intracortical microelectrodes have limitations for long-term use in the control of BMIs (Schwartz *et al* 2006, Wolpaw 2007, Nicolelis and Lebedev 2009, Hatsopoulos and Donoghue 2009, Chase *et al* 2010, Andersen *et al* 2010). On the other hand, intracortical local field potentials (LFPs) are thought to include both synaptic potentials and spiking activities of a large number of neurons around the recording electrode (Mitzdorf 1985, Katzner *et al* 2011, 2009, Lindén *et al* 2011), and recent studies showed that the LFPs include substantial information about movements (Pesaran *et al* 2002, Mehring *et al* 2003, 2004, Rickert *et al* 2005, Scherberger *et al* 2005).

The electrocorticogram (ECoG), as one of approaches to record neural activity, might be useful for long-term use in a BMI-application, if reasonable decoding performance could be obtained, because ECoG electrodes do not penetrate the cortical surface, thereby reducing the potential risk for brain tissue damage and increasing long-term stability for recordings in real-life (Chao *et al* 2010). In general, the ECoG involves the use of subdural, low-impedance, surface electrodes, typically spaced 1.0 cm apart, which are in common use for less invasive monitoring in human patients with epilepsy. These electrodes measure not only single or multiunit activities, but also synaptic inputs to a large population of neurons in the underlying cortical circuits and are thus considered to carry signals that are too coarse to pick up accurate signals decoding motor outputs. Recent studies have shown that ECoG signals carry rich information sufficient for decoding a limited set of discrete arm movements (Leuthardt *et al* 2004, Mehring *et al* 2004, Yanagisawa *et al* 2012). The potential advantages of the ECoG recordings over other less or non-invasive recording techniques might be that higher frequency signals are available in ECoG than in scalp EEG, because of their closer proximity to the surface of the brain, and that ECoG signals pick up neuronal signals from a large population of neurons in a wide area compared to the intracortical LFP that is recorded by electrodes with higher impedance. Thus, ECoG signals would be the transformed representations of intracortical LFPs across various depths of the cortex. Understanding the mechanism by which ECoG signals are generated is required not only to collect rich information from the brain for BMI-application, but also as an essential and important subject of neuroscience studies with a wide range of applicability. The relationship between ECoG signals and intracortical LFPs, however, remains largely unknown.

The present study aimed to reconstruct intracortical LFPs from ECoG signals recorded at the cortical surface. To compare the real and reconstructed LFPs, we simultaneously recorded subdural 32-channel ECoG signals and 64-channel intracortical LFPs from the primary motor cortex (M1) of a monkey performing reach-and-grasp movements. For the present study, we developed a novel electrode assembly, which enabled simultaneous recordings of neural signals from the cortical surface and various depths beneath the surface. The ECoG array is one module of the electrode assembly (Toda *et al* 2011b). A high-density electrode array with a regular grid was designed to enable detection of neural signals with sufficient information redundancy. Increasing information redundancy in the ECoG signals by overlapping with nearby ECoG electrodes was expected to lower the risk of poor construction of LFPs during the calculation process. Such high-density organization of the electrodes required smaller electrode-tips (50 μm $\times$ 50 μm) than the ECoG arrays usually used for clinical purposes.

Sparse estimation methods are expected to be useful for extracting significant information from redundant and numerous data in linear regressions for BMIs for brain activities (Ting *et al* 2008, Ganesh *et al* 2008, Nambu *et al* 2009, Toda *et al* 2011a). We used a sparse linear regression (SLiR) algorithm, which has a generalization capability for unknown datasets due to its ability to remove irrelevant features, avoid over-fitting of the datasets, and reduce calculation times, for the LFP construction.

Methods

All experimental procedures were performed in accordance with the Guidelines for Proper Conduct of Animal Experiments of the Science Council of Japan and approved by the Committee for Animal Experiment at the National Institutes of Natural Sciences. The data presented for all experimental sessions were obtained from a male Japanese monkey (*Macaca fuscata*; body weight of 7.4 kg).

Task

The monkey was trained to perform a single-handed reach-and-grasp task to capture a piece of food ($\sim$5 mm^3 apple cube) presented repeatedly in front of him by an experimenter. Over the entire experimental session, the food pieces were supplied around one position in a 3D workspace (figure 1(A)). The monkey reached for and grasped the food, brought his hand to his mouth, and ate the food. The monkey then placed his hand at the home position again and waited for several seconds. A piece of food was again presented in front of him and he reacted by reaching for it again. Such arm movements exhibited various trajectories across trials (figure 1(B)). The start times of reaching were not fixed in our experiments. There was no clear action epochs defined, such as reach–start–end or hand-rest, which were triggered by a go cue. However, roughly similar movements were repeated with about 8 s intervals (figures 1(C) and (D)). In each trial, we defined the 'reaching end point' as the spatial location where the hand reached the most distant point from the body axis (negative peaks in figure 1(C), middle panel). We defined 'reaching offset' as the time when the monkey reached the 'reaching end point'. An individual 'trial period' was defined as the period between 4 s before and 4 s after the 'reaching offset' (i.e. a total of 8 s/trial). For the selection of optimal LFP-channel subsets, movement- and rest-phases were defined as the periods between 1 s before and 1 s after the reaching offset, and the period between 3 s and 1 s before the reaching offset, respectively. The signals during these periods were used for checking whether the electrode picked up proper signals related to movement and rest (see below).

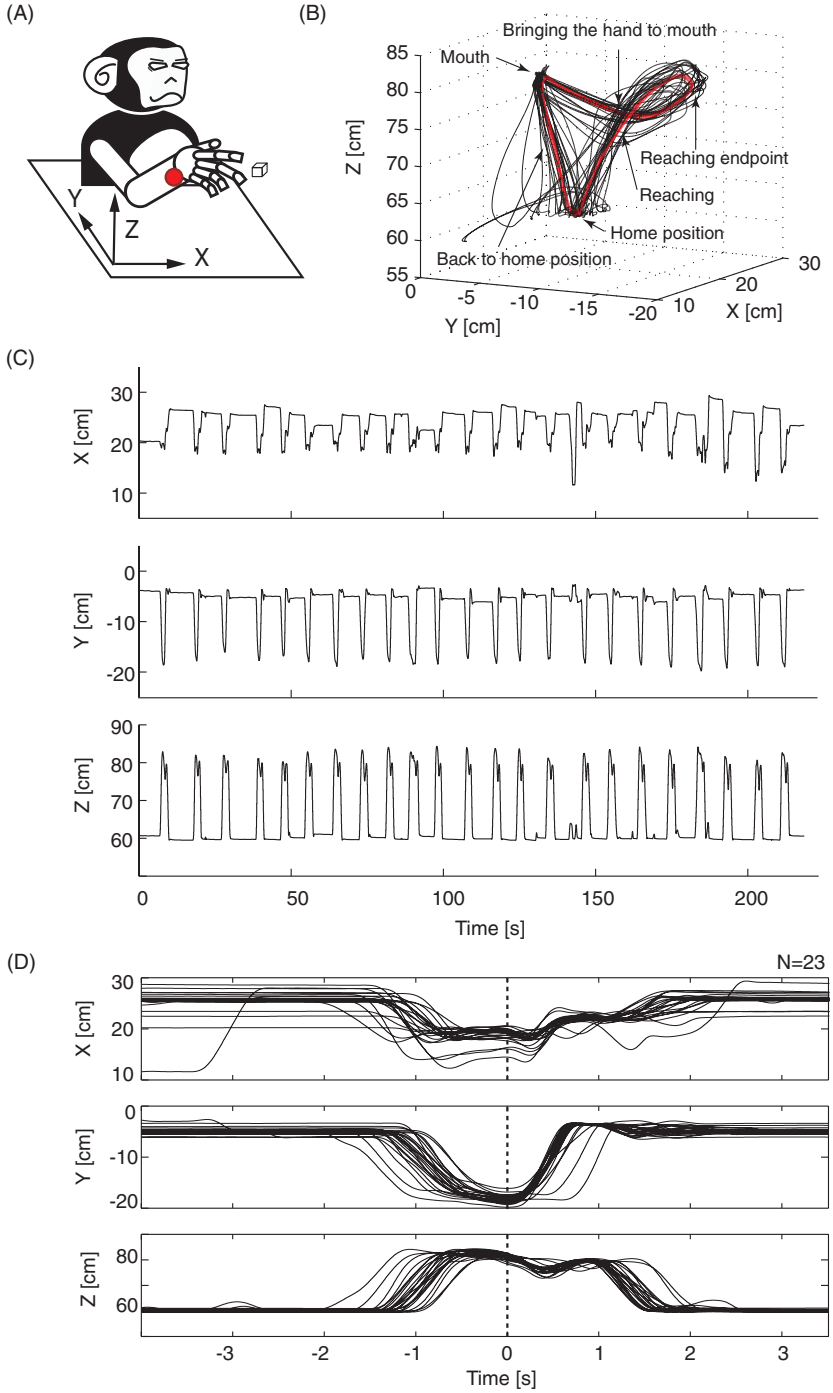

Figure 1. Free reach-and-grasp task. (A) A monkey performed reach-and-grasp movements to capture food pieces (open box close to fingertips) in a 3D free-workspace. A motion capture system recorded hand positions (measured at the wrist; red circle). (B) Superimposed trajectories of hand positions (black lines) in the 3D space over an entire single session (red line: averaged trajectory). The *x*, *y* and *z* axes are those indicated in panel (A). (C) Hand trajectories along each axis are shown for an entire single session containing 23 trials. The start timings of reaching were not fixed. (D) Superimposed trajectories of the hand along each axis during individual trials, aligned at the time of the 'reaching offset' (0 s), when the hand reached the most distant point from the body.

Recording of movement trajectories

The 3D position of the hand (measured at the wrist) across the reaching-space of the arm around the monkey was recorded using reflective markers tracked by an optical motion capture system (Eagle digital system; Motion Analysis Corporation, Santa Rosa, CA). The signals were synchronized with neural recordings through the hardware. The system used 12 infrared cameras operating at 200 frames/s to track the positions of multiple reflective markers (4-mm-diameter spheroids) with submillimeter accuracy. A total of nine markers were attached to the right forelimb of the monkey from the shoulder to the fingers. A kinematic model of the arm and hand was matched with the observed marker data using the system's software package (EVaRT 5.0.4) before analyzing the movement data. Sequential data of hand position in the orthogonal coordinate

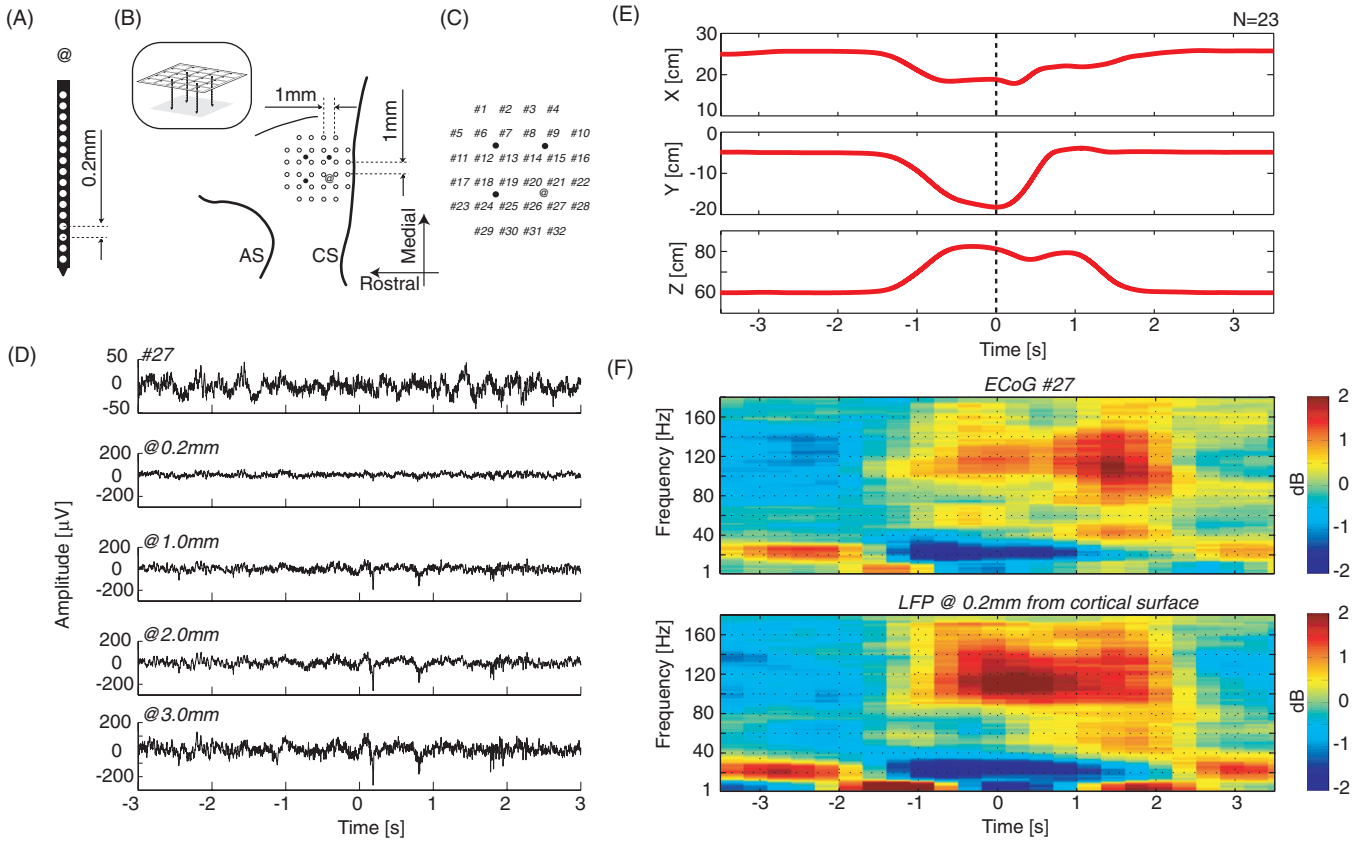

Figure 2. Electrode locations in the left primary motor cortex (M1) of the monkey and voltage traces recorded from the ECoG or intracortical electrodes. (A) A needle probe with linearly arranged 16-channel electrodes (open circles). The probes (400 μm diameter at the shaft) were inserted perpendicularly to the cortical surface into locations @ and the three other filled circles indicated in panel (B). (B) A schematic diagram of the electrode contact locations in M1 (open circle, regular-grid organization of the poly ECoG array; @ and three filled circles indicate the location of needle probes). CS, central sulcus; AS, arcuate sulcus in left hemisphere. (*Inset figure*) A schematic diagram of the 3D formation of the implantable electrode array. (C) Electrode indices of the ECoG array with the locations of each of the four electrodes shown in (B). (D) Examples of voltage traces of an ECoG signal (channel #27, *top*) and LFPs at various depths (0.2, 1.0, 2.0 and 3.0 mm) from the cortical surface recorded at probe @. Time zero corresponds to the 'reaching offset' (see (E)). (E) Averaged trajectories of the hand reaching along each axis. The most distant point of the hand from the monkey body (see the middle panel, along the *Y*-axis) was defined as 'reaching offset' point and set to time 0, when the hand reached the most distant point from the body. (F) Examples of averaged time-frequency analyses of an ECoG signal (*upper panel*) and an LFP (*lower panel*). The ECoG and LFPs were recorded from the cortical surface and at 0.2 mm from the surface, averaged over 23 trials in a single block, respectively. Time zero corresponds to 'reaching offset'.

system (figure 1(B)) were linearly interpolated and then filtered (low pass with cutoff edge at 10Hz) in each orthogonal coordinate axis. In addition to the optical data, the motion capture system also recorded the analog signals from the external stimulator (SEN-8203; Nihon Kohden Corporation, Tokyo, Japan) as the synchronized time-stamped data with neural recordings. The motion data were then up-sampled to 500 samples per second to match the neural data.

Implantable 3D electrode array

We designed a novel probe for chronic cortical recordings. This probe was an assembly constructed with two modules, a micro-ECoG array and multi-channel needle probes (inset of figure 2(B)).

Micro-ECoG electrode array

Multichannel electrode arrays for ECoG recordings made of poly (chloro-para-xylylene, Parylene-C) were developed (Toda *et al* 2011b). A parylene-gold-parylene sandwich structure achieved flexibility of the electrode array. The 32-channel electrode array was arranged in regular grids (50 μm $\times$ 50 μm with a 1 mm inter-electrode distance, figures 2(B) and (C)). A platinum-black coating of individual electrodes yielded an impedance of $\sim$10 kΩ in saline at 1 kHz. The array consisted of a mesh-like structure; 5 $\times$ 5 square holes (800 $\times$ 800 μm for each) were open in the space between electrodes. The size of the entire 6 $\times$ 6 micro-ECoG electrode array was 5 $\times$ 5 mm square. Four silver-wires (300 μm in diameter; over 5 cm length) were used as reference electrodes (see below).

Multi-channel needle probe

Sixteen-channel platinum electrodes (Unique Medical Corporation ltd, Tokyo, Japan) were linearly mounted on a needle probe (400 μm in diameter; 4.5 mm length from apical to basal tip). The diameter and electrochemical impedance of each individual electrode-tip was about 30 μm and

400 kΩ in saline at 1 kHz, respectively. Inter-electrode distance was 200 μm and the terminal electrode in the single linear arrangement of electrodes was located 200 μm from the proximal tip of the probe (figure 2(A)). Each needle probe was vertically inserted through one of the holes of the micro-ECoG electrode array (figure 2(B)). Basal tips of the needle probes were bound to the micro-ECoG electrode array with a silicon membrane (200 μm thick). In other words, the deepest electrodes were located 3.2 mm from the cortical surface when the electrode assembly was implanted into the subdural space overlying the cerebral cortex. Because the superstructure segment of the electrode assembly was made of silicon membrane and flattened, the pressure from the dura was uniformly distributed, and we could avoid extra pressure impinging on the electrode assembly being transmitted to the brain parenchyma after the surgery. The electrode assembly, as an implantable probe array, enabled chronic neural recording from intracortical locations at various depths and from the cortical surface.

Surgery for implanting the electrode assembly

The electrode assembly was chronically implanted in the monkey's left primary motor cortex (M1) under anesthesia. As premedication, dexamethasone (0.20 mg kg^{-1}), atropine sulfate (33×10^3 μg kg^{-1}) and penicillin potassium (2.5×10^3 units kg^{-1}) were injected intramuscularly. Anesthesia was introduced with intramuscular injections of ketamine (1.0 mg kg^{-1}) and xylazine (0.5 mg kg^{-1}). During the surgery, anesthesia was maintained with inhalation of 1–2% isoflurane, and electrocardiogram, PCO_2, and arterial O_2 levels were continuously monitored. Cerebral edema was prevented by Mannitol (20w/v%) application through the venous line. A craniotomy was performed above M1, and the dura was incised and reflected. The electrode array was positioned on the rostral bank of the central sulcus, the hand/arm area of M1. The dura was closed using 6.0 synthetic absorbable suture threads within surgical glue composed of gelatin after two silver-wires as reference electrodes were inserted to the subdural space. A piece of artificial dura mater was applied over the dura and two reference electrodes were inserted into supradural space between the dura and the skull. The craniotomy was closed with a piece of dental acrylic. Head holders were attached to the skull. Finally the skull was coated with dental acrylic. After termination of the surgery, diclofenac sodium (25 mg; Voltaren, Novartis Pharma K.K., Tokyo, Japan) was applied anally for analgesia.

Neural recording

Recording sessions were initiated 11 days after the surgery. Neural data were collected using an acquisition processor system (Plexon, Inc., Dallas, USA). The head of the monkey was fixed to the monkey chair during recording. The LFPs were originally filtered on-line with 0.7 Hz high-pass and 8 kHz low-pass analog filters and sampled at 20 000 samples per second. Both the hand position data from the motion capture system and the data of the neural activity received synchronized signals for *post hoc* matching of the time-lines between them. A band-pass filter (1–250 Hz) was applied off-line to the measured data before it was down-sampled to 500 samples per second to match the movement data.

Data analysis

All data analyses were performed using Matlab (The Mathworks, Inc., Natick, MA, USA). We primarily used the MATLAB functions 'anovan' and 'anova1' in analysis of variance (ANOVA). Additionally, three-way mixed ANOVA was performed in SPSS for Windows (SPSS Inc., Chicago, Il, USA). Comparisons among groups were conducted by applying the Tukey–Kramer test. The statistical significance was assessed at a 5% or 1% confidence level by using the F test. We evaluated the quality of fit from the correlation coefficient (r) in regression analysis. All data are expressed as the mean and standard deviation (SD) in sample data number, unless otherwise noted.

Selection of optimal channel subsets for the LFP recordings

We made simultaneous recordings of LFPs from 64-channel intracortical electrodes and ECoGs from 32-channel electrodes. Motion-related signals in all of the 96-channel recording signals were analyzed. Some channels appeared to pick up movement-related signals properly, while others did not. To select appropriate channels related to the reaching movements for analysis and to exclude others, we focused on modulations of the β band (10–35 Hz) and high-γ band (80–170 Hz) components relative to the movements. As shown in figures 2(E) and (F), the β band component was dominant during the preparatory period, and then ceased at the time to move. In contrast, the high-γ component was dominant during the dynamic phase of movement (Ohara *et al* 2001, Marsden *et al* 2000, Crone *et al* 1998 with human ECoG). Signals of all channels were first examined by time-frequency analysis (see the following section, *Spectral analysis*) and then those recorded signals whose power-variances in the β and high-γ band components were significantly modulated by arm movements were defined as recorded from the 'intact' channel and used for further analysis. The statistical differences were determined by paired t-test, with $P < 0.01$ considered significant. Forty-two of the 64 intracortical electrodes exhibited significant increases in the power-variances of the high-γ band signals between the resting and movement phases. Among them, 41 channels exhibited significant decreases in the power-variances of the β band signals between the resting and movement phases. Of the two anterior probes (two filled circles on the left side in figure 2(B)), physiologically relevant signals deeper than 2 mm were recorded from only five channels. Signals recorded from all of the 32 ECoG channels showed modulation of both the β and high-γ bands. Therefore, we used the 41 intracortical LFPs (five channels from each of the rostral two probes, 16 channels from the medial caudal probe, and 15 channels from the @ caudal probes) and 32 ECoG signals for analysis of movement-related signals. A one-way ANOVA with multiple comparison test between the medial caudal probe and the @ caudal probes revealed that the

power-variances of the high-γ band signals of LFPs of probe @ were significantly larger than those of the other probes ($P < 0.01$), while there was no significant difference in the β band signals ($P > 0.5$).

Reconstruction of the LFP from the ECoG signals

To reconstruct the intracortical LFP from the 32-channel ECoG signals, we applied a SLiR algorithm, which has a generalization capability for unknown datasets due to its ability to remove irrelevant features (Nambu *et al* 2009, Toda *et al* 2011a). The reconstructed LFP, u, at time t is described as

$$u(t) = \sum_{i=1}^{N} \sum_{j=0}^{M} w_{ij} x_i (t - j\Delta),$$

where $x_i(t)$ is the ECoG signal of channel i at time t, and Δ is a discrete-time step-size of 10 ms. w_{ij} is a weight for the ith ECoG electrode at the time lag $j\Delta$, a so-called weighting coefficient. LFP signals were computed from all of the preceding ECoG signals ($N = 32$) at a time point within a temporal window corresponding to the whole of the time lag ($M = 99$). The regression process was performed at each time point, t, of the data. The interval of time points in our neural data for the regression was 2 ms and the reconstructed signals allowed the temporal resolution as with the real signals (500 Hz). In general, the lags in the linear summation process can be either negative (in the past) or positive (in the future) with respect to the present time t. Here, we considered only the lags of the past (-1 to 0 s).

The accuracy of the LFP reconstructed from the ECoG was evaluated using the cross-validation scheme. The SLiR algorithm determined the weighting coefficients from the training dataset, and the performance of the reconstruction was examined on the test data not used for the training to estimate the weights (22 trials for the training data and one trial for the test data in each session). To assess the reconstruction performance of the SLiR with the three frequency ranges as motion-related signals—the broadband (1–250 Hz), the β band (10–35 Hz) and the high-γ band (80–170 Hz)—we determined weighting coefficients from a filtered dataset for each frequency range.

To evaluate the accuracy of the reconstructed LFP, the correlation coefficient (r) was calculated between the real and reconstructed LFPs and a repeated 23-fold cross-validation was used to evaluate the accuracy. Moreover, the SLiR model determined from all the data within the session was then applied to another dataset (novel dataset), and the correlation coefficients of the novel dataset were used to evaluate the accuracy of the reconstructed LFP. This double assessment of the generalization capability of the SLiR algorithm was performed because possible applications of the proposed method to decode the motor output will require learning generalization across different experimental sessions.

The effect of sparseness for reconstructing the LFP with SLiR was evaluated by comparison with the ordinary linear regression method, which omitted sparse function from SLiR. Accuracy of the reconstructed LFP using ordinary linear regression method was calculated in a similar manner as the SLiR mentioned above.

Spectral analysis

The time-frequency analysis enabled us to identify the temporal dynamic features of the LFP signals. The analysis was performed on a session using the discrete multitaper method, using non-overlapping, sliding windows of 300 ms. The power variability at each frequency was assessed across the non-overlapping time windows during a given session, using a relative quantity of variability given by the power, p, for a channel i at each frequency, f (frequency resolution 1 Hz), in dB, defined as $10\log_{10}\{p_{i,f}/\mathrm{mean}(p_{i,f})\}$, because the LFP power values across different frequencies can differ by orders of magnitude. The spectral regions over 250 Hz were outside of the Nyquist frequency range of data sampling.

Exponential curve-fitting to temporal structure of weight values

To evaluate the temporal structure of weight values for the reconstructed LFP, the profile of the magnitude was represented as the root-mean-square (RMS) of their values, and fitted to a single exponential curve ($y = Ae^{-t/\tau}$) by the least-squares method. Parameter values, amplitude (A) and decay constant (τ) were provided by fitting with a single exponential curve. Ratio of the power for the earlier weight RMS values from -1 under 0 s ($t = (-1\ 0)$) versus all weight RMS values from -1 to 0 s, which included current RMS value just at 0 s ($t = (-1\ 0]$), was calculated from the fitting exponential curve. The power ratio of the past RMS gives a comprehensive explanation of the temporal structure of weight values. Higher ratio of the power indicated stronger contribution of the past ($t = (-1\ 0)$) information than the current ($t = 0$) information to reconstruction of the LFPs.

Results

ECoG signals and LFP profiles at various depths in the motor cortex

We focus here on the LFP signals of the probe @ (figures 2(A)–(C)), because this probe included the largest number of the 'intact' LFP channels as judged by the power-variances of high-γ band signals at the deepest position among the four probes (see the methods section). Results of simultaneous recordings from representative channels of ECoG and LFPs at various depths during a single trial of the arm movement are exemplified in figure 2(D). The results indicated that the ECoG signal recorded close to the surface point of the needle probe was similar to the LFPs recorded just below (0.2 mm) the ECoG electrode (figure 2(F)). However, as the depth increased, the LFPs appeared to become increasingly different from the ECoG signals recorded above them.

Figure 2(F) shows the averaged spectrograms of movement-related neural activity from ECoG #27 (upper panel) and the LFP probe @ at a depth of 0.2 mm (lower panel). While the monkey kept his hand at the home position, the β band component (10–35 Hz) was high and then exhibited a negative deflection at -2 to -1 s. Movements typically

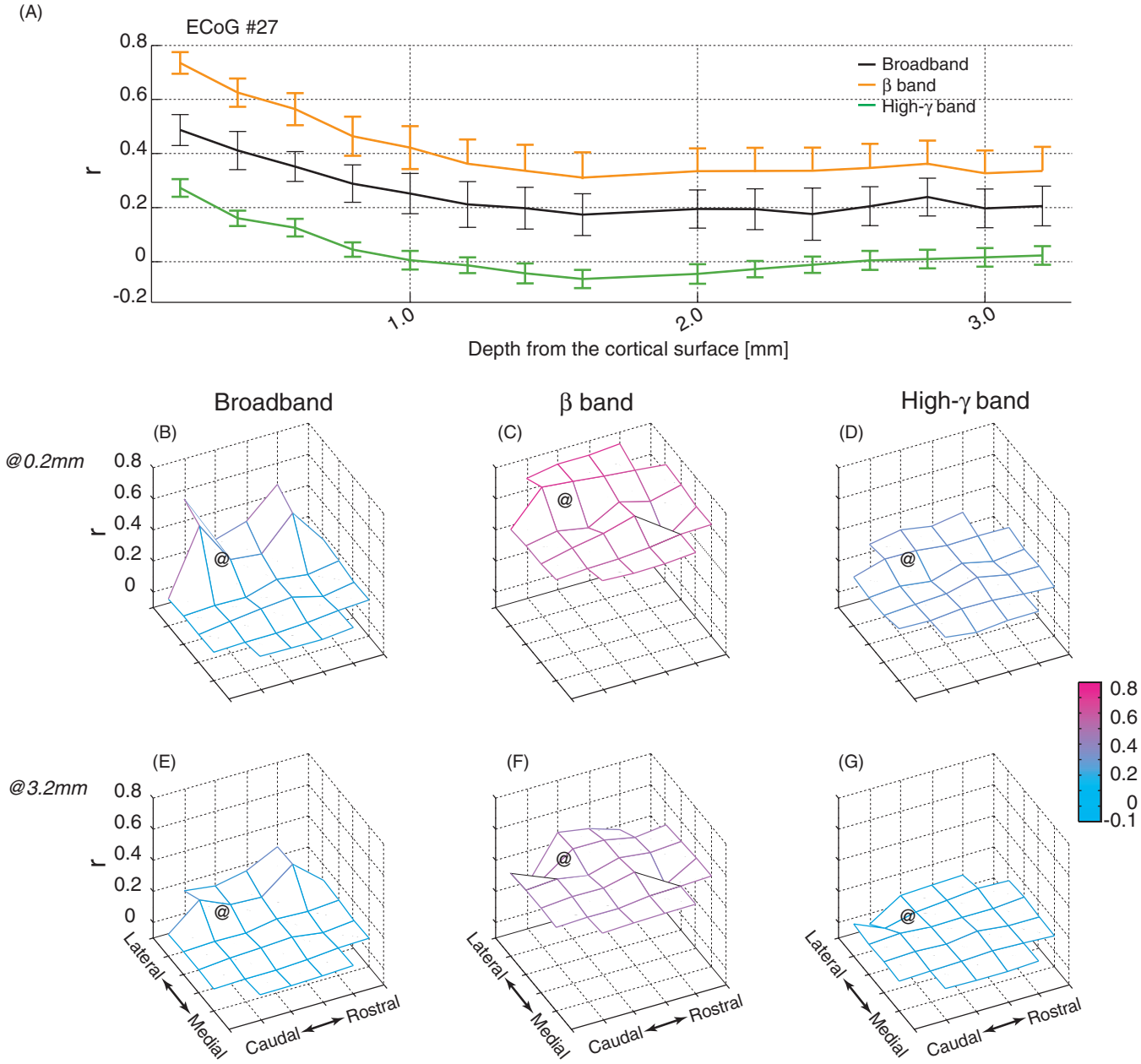

Figure 3. Correlations between the voltage profile of LFPs and the ECoG signals recorded just above them in different frequency ranges. LFPs were recorded from the needle probe @ (see figures 2(B) and (C)). (A) Correlation coefficients (r) between the LFPs at different depths of the probe @ and the #27 ECoG signal (one of the closest channels to the needle probe) at different frequency ranges: broadband (black), β band (red), and high-γ band (blue). Note that the correlation with the ECoG declined sharply as the depth increased, especially for the high-γ component (blue) of the LFP signal. Error bars indicate SD obtained from the 23-fold cross-validation sets. (B–G) Average correlation coefficients between ECoG signals and LFPs at 0.2 mm (B–D) and 3.2 mm (E–G) from the cortical surface of probe @ at different frequency ranges: broadband (B, E), β band (C, F) and high-γ band (D, G). Positions of individual ECoG electrodes correspond to intersection points on the mesh grid.

started 1.5 s before the reaching offset, and were associated with decreases in lower-frequency components and increases in higher frequency components, including the high-γ (80–170 Hz). The increase in the high-frequency components and decrease in the low-frequency components occurred for the duration of the arm-movement, and were subsequently followed by an increase in the low-frequency component at ~3 s, when the monkey put his hand back at the home position.

Figure 3(A) shows average correlation coefficients between LFPs of the probe @ and the signal from the #27 ECoG channel at different frequency-band components as a function of the LFP channel-depth. At 0.2 mm, the β band signal exhibited a relatively high correlation with the ECoG signals recorded in the nearby proximity (probe @ with ECoG channel #27; $r = 0.73 \pm 0.03$ for 23 trials in a single session). In contrast, the correlation coefficients of the high-γ band signals at the same recording sites were very low ($r = 0.27 \pm 0.03$). As the depth increased, correlations of the ECoG signals with the LFP signals from probe @ decreased, especially in the high frequency component. At 3.2 mm below the cortical

surface, the correlation coefficient of the β band component was still 0.33 $\pm$ 0.08, while that of the high-γ component was nearly 0 below a depth of 0.8 mm. Similar results were obtained with other proximal ECoG channels, including #26, #20 and #21 (data not shown). These were low correlations even between the closest pairs of ECoG channels and LFPs.

Spatial profiles of correlation coefficients between a LFP signal and ECoG on the cortical surface were non-uniform (figures 3(B)–(G)). The correlation coefficients of the β band component were higher than those of the high-γ component; the ECoG signals at the high-γ frequency range were only poorly correlated with LFPs at all positions (figures 3(C), (D), (F) and (G)). The β-frequency component of the ECoG signals recorded from the lateral area of the array showed a positive correlation with superficial LFPs (figure 3(C)). We analyzed the correlation coefficients with a three-way mixed ANOVA (the three frequency bands $\times$ depths of LFP channels $\times$ horizontal distances between the LFP probe and ECoG channels) to examine possible interactions among these main effects. Although there were significant two-way interactions (frequency $\times$ depth: $\varepsilon_{GG} = 0.793$, $F(14, 21\,840) = 37.21$, $P < 0.001$; $\varepsilon_{GG} = 0.793$, frequency $\times$ distance: $F(14, 21\,840) = 75.06$, $P < 0.001$; distance $\times$ depth: $F(98, 10\,920) = 2.40$, $P < 0.001$), there was no significant three-way interaction ($F(196, 21\,840) = 0.13$, $P = 1$). Thus, the spatial distribution of correlations between the ECoG (broadband (1–250 Hz) and β band) and LFP signals was non-uniform. The high-γ band component of the ECoG signals exhibited a weak or virtually no correlation with the LFPs for all recording sites.

Reconstruction of LFPs with SLiR

To reconstruct the intracortical LFPs from the 32 ECoG signals, we applied a SLiR algorithm. In this reconstruction process, we tested both spatial and spatiotemporal weighted summations (table 1). The former used the ECoG signals without introducing a time lag, and the latter used the ECoG signals in the time window (−1 to 0 s). Then, a three-way ANOVA (frequency bands, depths of LFP channels, and type of weighted summation) revealed a significant three-way interaction (frequency $\times$ depth $\times$ summation: $F(30, 124\,380) = 107.7$, $P < 0.01$) and all possible three-way interactions (frequency $\times$ depth: $F(30, 124\,445) = 287.1$, $P < 0.01$; frequency $\times$ summation: $F(2, 124\,473) = 1015.4$, $P < 0.01$; summation $\times$ depth: $F(15, 124\,460) = 345.4$, $P < 0.01$). Furthermore, the spatiotemporal weighted summations provided better reconstructions across the 41 LFPs than the spatial weighted summations ($P < 0.01$). Multiple comparison tests identified differences among the broadband, β band, and high-γ component signals in each of the spatiotemporal and spatial weighted summations ($P < 0.01$). Figure 4 shows the results of reconstructing LFPs recorded at various depths of probe @ (figures 2(B) and (C)). The SLiR resulted in a fairly good reconstruction of the intracortical LFPs from the 32-channel ECoG signals, with a correlation coefficient of 0.7 at a depth of 0.2 mm when the spatiotemporal weighted summations were used. Surprisingly, when we focused on the LFP signals of probe @, the reduction in the reconstruction accuracy was moderate even though the depth increased ($r = 0.59$ at a depth of 3.2 mm; figure 4(B)). When we used just the spatial weighted summation, the reconstruction accuracy was significantly lower ($P < 0.01$). The correlation coefficient was 0.72 for the depth 0.2 mm and 0.49 for the depth 3.2 mm (blue traces in figures 4(A) and (B)).

When different frequency components were analyzed separately, both the β band and the high-γ components of the LFP signals were fairy well reconstructed from the ECoG signals (figures 4(C)–(E)). The highest correlation coefficients were at the most superficial channel (at 0.2 mm, $r = 0.77 \pm 0.02$, 0.79 ± 0.02 and 0.41 ± 0.02 for the broadband range, β band and high-γ band components, respectively). The values did not decline much at the deeper electrodes in the broadband and β band range (at 3.2 mm, $r = 0.56 \pm 0.03$, 0.57 ± 0.04 and 0.15 ± 0.03 for the broadband range, β band and high-γ band components, respectively). As shown in figures 4(C)–(E), the spatiotemporal weighted summation obtained by the SLiR with multiple ECoG signals contributed to a higher quality of reconstruction accuracy on LFP profiles at all depths along the probe for the broadband, β band and high-γ band components.

Weighting coefficients for the LFP reconstruction

With the spatiotemporal weighted summation, the LFP signals at various depths in the cortex were reconstructed from the 32-channel ECoG signals obtained in the 1 s time window (figures 5(A) and (B)). Through the calculation process to reconstruct the LFPs with the SLiR algorithm, ineffective ECoG channels were identified as null-weights over the entire time window. Figures 5(A) and (B) show the weights of the signals from the individual ECoG channels; many of the channels were judged to be ineffective for reconstructing LFPs during the calculation process. ECoG channels close to the LFP probe (close to the top of figures 5(A) and (B)) tended to be judged as effective. In figures 5(E)–(G), remote ECoG channels located more than 2.5 mm away from probe @ are indicated in blue. Figure 5(E) shows that mainly ECoG channels close to probe @ were used for reconstructing LFP signals at a depth of 0.2 mm. In contrast, as shown in figure 5(F), not only the close channels, but also remote channels were effective for reconstructing LFP signals at 3.2 mm. To quantify how much the remote ECoG channels contributed to reconstructing the LFPs at various depths, the data were analyzed by one-way ANOVA followed by multiple comparison tests. There were significant differences in the numbers of effective ECoG channels (among all the channels and among only the remote channels) required to successfully reconstruct LFPs at different depths ($P < 0.01$, ANOVA); the number of effective-ECoG channels used at 3.2 mm was significantly larger than that at 0.2 mm ($P < 0.01$) from among all channels and from among only the remote channels (figure 5(G)). Thus, reconstructions of deeper LFPs tended to require a larger number of the ECoG channels.

To evaluate the temporal structure of weight values, the profile of their magnitudes was fitted by a single exponential curve (figures 5(C) and (D)). The exponential curve-fitting

Table 1. Summary of reconstruction accuracies in the 41 LFP channels.

Depth (mm) (number of intact channels)		0.2 (3)	0.4 (4)	0.6 (3)	0.8 (3)	1.0 (4)	1.2 (2)	1.4 (3)	1.6 (2)	1.8 (2)	2.0 (2)	2.2 (3)	2.4 (2)	2.6 (2)	2.8 (2)	3.0 (2)	3.2 (2)	All (41)
Spatiotemporal	Broadband	0.66 ± 0.11	0.60 ± 0.05	0.68 ± 0.05	0.58 ± 0.04	0.60 ± 0.06	0.56 ± 0.06	0.52 ± 0.05	0.54 ± 0.04	0.49 ± 0.08	0.50 ± 0.09	0.53 ± 0.05	0.44 ± 0.08	0.56 ± 0.04	0.56 ± 0.04	0.45 ± 0.09	0.55 ± 0.04	0.56 ± 0.09
weighted	β band	0.76 ± 0.04	0.70 ± 0.04	0.72 ± 0.05	0.64 ± 0.05	0.62 ± 0.07	0.60 ± 0.06	0.59 ± 0.07	0.57 ± 0.04	0.53 ± 0.05	0.55 ± 0.05	0.54 ± 0.06	0.47 ± 0.11	0.57 ± 0.05	0.56 ± 0.05	0.48 ± 0.09	0.55 ± 0.04	0.60 ± 0.10
summation	High-γ band	0.32 ± 0.07	0.24 ± 0.04	0.25 ± 0.03	0.22 ± 0.08	0.18 ± 0.05	0.15 ± 0.04	0.17 ± 0.06	0.13 ± 0.02	0.13 ± 0.04	0.12 ± 0.03	0.12 ± 0.04	0.15 ± 0.02	0.15 ± 0.04	0.15 ± 0.04	0.11 ± 0.04	0.14 ± 0.03	0.18 ± 0.07
Spatial	Broadband	0.58 ± 0.14	0.54 ± 0.06	0.61 ± 0.06	0.50 ± 0.04	0.51 ± 0.06	0.46 ± 0.07	0.39 ± 0.06	0.42 ± 0.04	0.37 ± 0.08	0.37 ± 0.07	0.41 ± 0.05	0.30 ± 0.09	0.43 ± 0.04	0.43 ± 0.04	0.33 ± 0.07	0.42 ± 0.04	0.46 ± 0.11
weighted	β band	0.73 ± 0.04	0.66 ± 0.04	0.67 ± 0.05	0.57 ± 0.05	0.53 ± 0.07	0.50 ± 0.07	0.47 ± 0.06	0.44 ± 0.05	0.41 ± 0.05	0.42 ± 0.06	0.40 ± 0.07	0.36 ± 0.11	0.43 ± 0.06	0.43 ± 0.07	0.36 ± 0.10	0.41 ± 0.07	0.51 ± 0.13
summation	High-γ band	0.25 ± 0.05	0.18 ± 0.04	0.18 ± 0.03	0.13 ± 0.05	0.12 ± 0.04	0.09 ± 0.03	0.10 ± 0.04	0.08 ± 0.02	0.08 ± 0.03	0.08 ± 0.02	0.08 ± 0.03	0.06 ± 0.05	0.09 ± 0.03	0.09 ± 0.03	0.07 ± 0.03	0.09 ± 0.02	0.12 ± 0.06

Values are the mean correlation coefficients between real and reconstructed LFP across the 23-fold cross-validation trials (± SD).

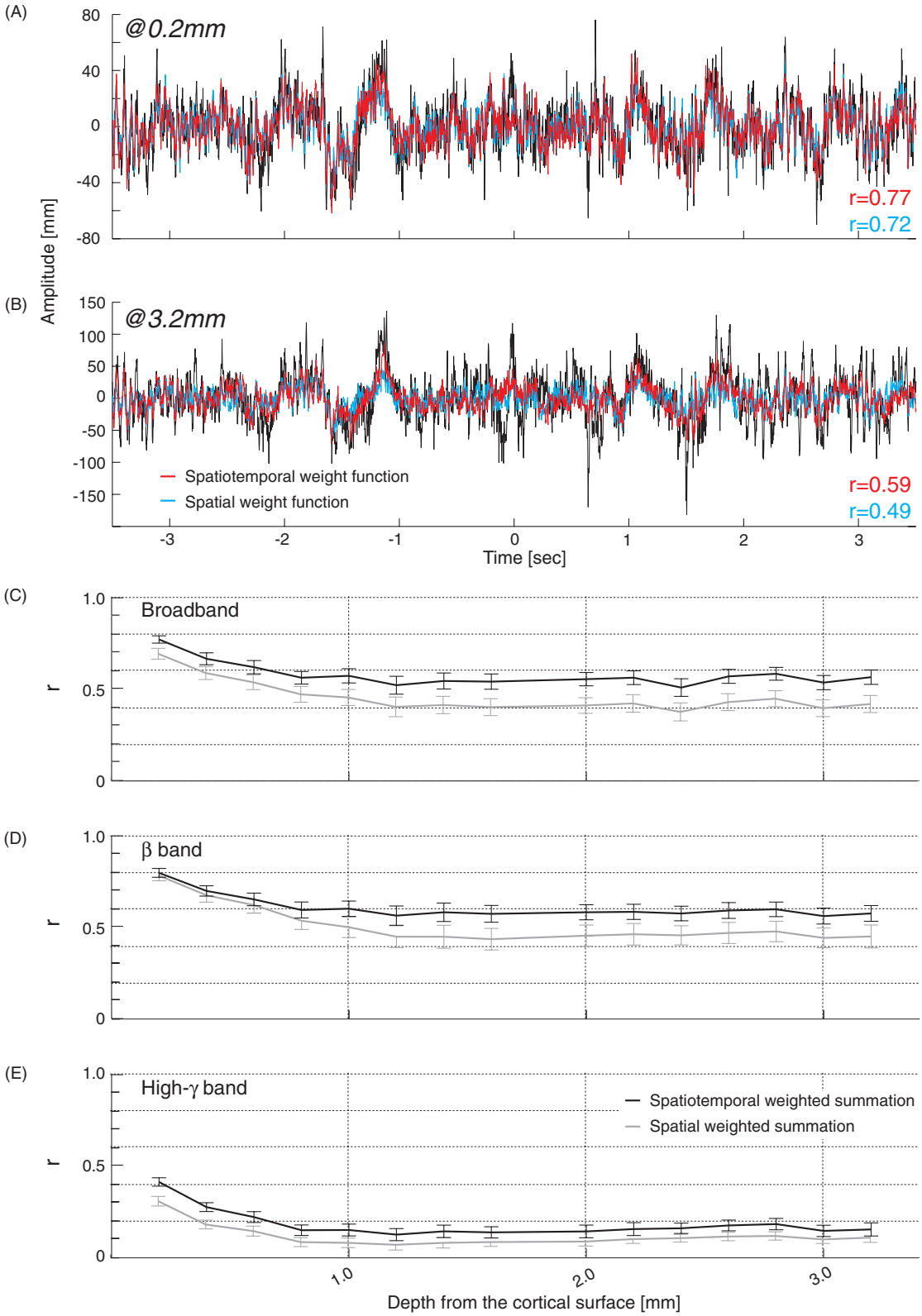

Figure 4. Performance of the LFPs reconstructed from the multi-channel ECoG signals using the SLiR. (A and B) Examples of the reconstructed LFPs recorded at the depths 0.2 mm (A) and 3.2 mm (B). Broadband (1–250 Hz) LFP signals were reconstructed by weighted summations of the 32 ECoG signals. Correlation coefficients between the real (black) and reconstructed voltage profiles using spatiotemporal weighted summations (red) were lower than those reconstructed using spatial-weighted summations (blue). (C–E) Depth profiles of the performances for reconstruction. Correlation coefficients between the real and reconstructed LFPs at various frequency ranges: broadband (C), β band (D) and high-γ band (E) in probe @ were averaged over 23-fold cross-validation trials (error bars indicate SD). There are significant differences in the correlation coefficients obtained by predictions with spatiotemporal (black lines) and spatial (tone lines) weighted summations at each depth and for all frequency ranges.

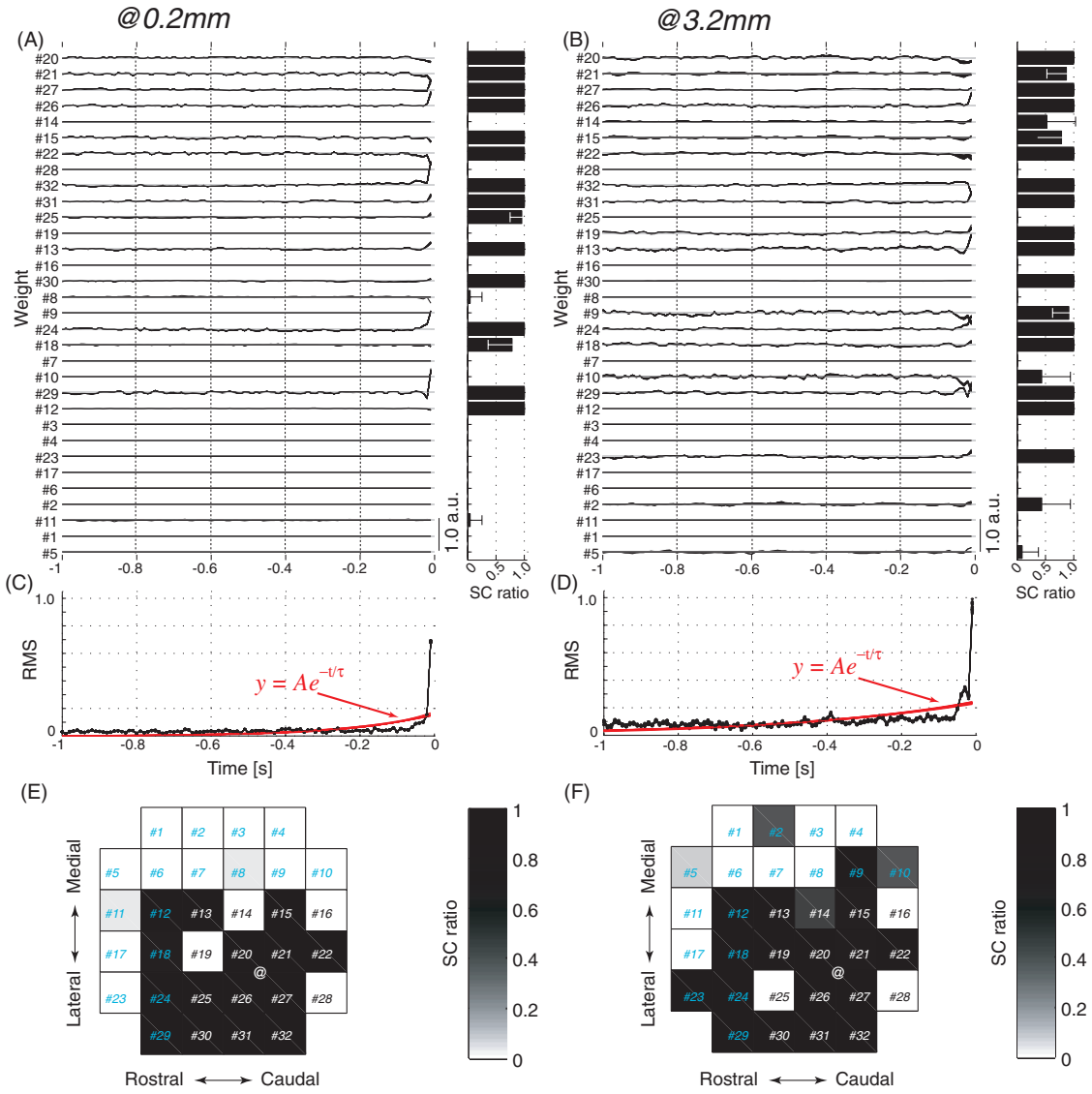

Figure 5. Spatiotemporal weighted summations for reconstructing LFPs with the SLiR. (A and B) Temporal profiles of regression weights for ECoG signals at each of the 32 channels at depths of 0.2 mm (A) and 3.2 mm (B). (*Left panels*) Amplitude of the LFP at time zero was reconstructed by the 32 weighted ECoG signals during the preceding 1 s. The order of the channel index of ECoG signals is associated with their distances to needle probe @ (the closest ones are indicated at the *top*, see figure 2(C)). Multiple lines at each trace indicate variations in the weighted summation with 23-fold cross-validation. The vertical scale bar indicates 1.0 arbitrary unit (a.u.) for calculation of the real LFP signal scale. (*Right panels*) The average selection count (SC) of effective channels determined by the SLiR for reconstructing LFPs across the 23-fold cross-validation trials is defined as the SC ratio and plotted on the horizontal axis for each ECoG channel. Ineffective ECoG channels were assigned a null regression weight in the entire time window. An SC ratio of 1.0 indicates that the corresponding ECoG channel was used for reconstructing LFPs in all of the 23 cross-validation trials. Error bars indicate SD. (C and D) Time courses of weight values. Root mean squares (RMS) of the weight values across the 23 cross-validation trials are indicated along the vertical axis. Red lines correspond to fitting with exponential functions ($y = Ae^{-t/\tau}$). Parameter values of the functions, amplitude (A) and the decay constant (τ), were estimated from the time courses of weight values in each cross-validation trial. (E and F) Distributions of effective ECoG channels. The results of the right panels in (A) and (B) were replotted two-dimensionally to better illustrate the relationship between the locations of effective ECoG channels and that of probe @. The SC ratios are grayscale-coded corresponding to the ratios in (A) and (B). Channel numbers with blue fonts indicate remote ECoG channels. (G) The number of effective ECoG channels for reconstructing LFPs at different depths of probe @, taking into consideration all channels (black line) and only remote channels (blue line) in the ECoG array. (H and I) Values of parameters A and τ for reconstructing the LFPs at different depths. (J) Contribution of past information for reconstructing LFPs. The ratio of the power for the earlier RMS values versus all RMS values is plotted for reconstructing LFPs at individual depths. (*Inset panel*) Ratio of the power for earlier RMS values (black area; the weighted summations from −1 under 0 s) and current RMS value (gray area; weight amplitude just at 0 s). Error bars indicate SD ($n = 23$).

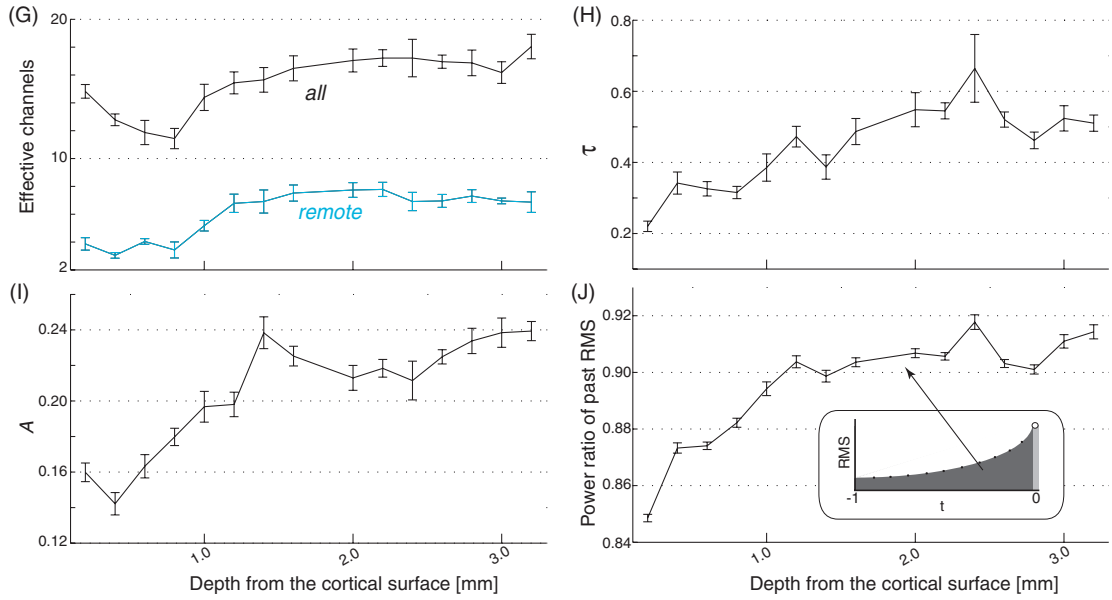

Figure 5. (Continued.)

demonstrated that more recent ECoG signals tended to contribute more to the reconstruction of LFP signals (depth 0.2 mm, $A = 0.15 \pm 0.05$, $\tau = 0.21 \pm 0.01$, MSE $= 0.06 \pm 0.001$; depth 3.2 mm, $A = 0.23 \pm 0.05$, $\tau = 0.51 \pm 0.02$, MSE $= 0.08 \pm 0.02$). There were significant differences in both the amplitude (A) and the decay constant (τ) of the exponentially fitted curves ($P < 0.01$, ANOVA) between the LFP records at 0.2 mm and those at 3.2 mm. Both of these parameters exhibited an increasing trend along with the depth of the reconstructed LFPs (figures 5(H) and (I)). The past RMS powers also increased significantly in proportion to the depths from the cortical surface (figure 5(J)). This indicated that older information from the ECoG signals tended to have a larger contribution to reconstructions of deeper layer LFPs. Mean square error of the exponentially fitted curve also increased with the depth of the reconstructed LFPs (∼0.06–0.08).

Reconstruction of brain activity during arm movements

Throughout the reconstruction process, the question arose as to whether the LFP signals reconstructed with the SLiR carried meaningful information related to the arm movements of the monkey. To address this question directly, the weighted summations obtained from the training dataset were then applied to novel datasets that were obtained through a session of sequential reach-and-grasp trials as well as from training and test datasets that were not used for calculating the weighted summations. In the novel data, the monkey's arm movements and the time at which to start reaching were also not fixed in our experiments (figures 6(A) and (B)). A time-frequency analysis revealed that the reconstructed LFP signals from the weighted summations represent the neural activity that is associated with the monkey's arm movements in the novel datasets. Similar to the time-frequency analysis data of the real LFP recordings at 0.2 mm (figure 6(C)), the high-γ band activities and β band activities appeared alternately in the reconstructed LFP during the action-phases for reaching and during rest-phases when the hand was kept at the home position, respectively (figure 6(D)). Similar alternations of β and high-γ band signals relative to arm movements were also represented in the LFPs reconstructed from the electrodes at 3.2 mm (figures 6(E) and (F)). Correlation coefficients between the real and reconstructed time-frequency analyses (figures 6(G) and (H)) revealed that the linear regression method accurately reconstructed the LFP signal components with frequencies lower than 150 Hz. In particular, the power of reconstructed LFP at 15–30 Hz (belonging to β band) and 110–140 Hz (belonging to high-γ band) appeared to accurately represent the real LFP signals. It raises possibility that the frequency components within the β and high-γ ranges of the reconstructed LFPs were useful for identifying the arm-movement phase in our experiments. The time-frequency analysis appeared to clearly discriminate the individual phases of the arm movements. Moreover, the accuracy of the SLiR was significantly higher than that of an ordinary linear regression method ($P < 0.01$, paired t-test), suggesting that the SLiR algorithm might be useful for a real-time BMI application.

Discussion

In this study, we found that the waveforms of single ECoG signals on the surface of the cerebral cortex are similar to the intracortical LFPs close to the surface, especially for the lower frequency component (β band); however, they did not resemble the deeper layer LFPs. The correlation coefficient of the higher frequency component (high-γ band) declined sharply as the depth increased. However, multi-channel micro-ECoG array allowed us to reconstruct LFPs with high accuracy even at a depth of 3.2 mm by applying the SLiR algorithm. Estimating intracortical activity from surface recordings is an important subject in contemporary neuroscience studies (Whittingstall and Logothetis 2009). Detection of high-γ band component with subdural ECoG array is important for estimation of intracortical neural activity

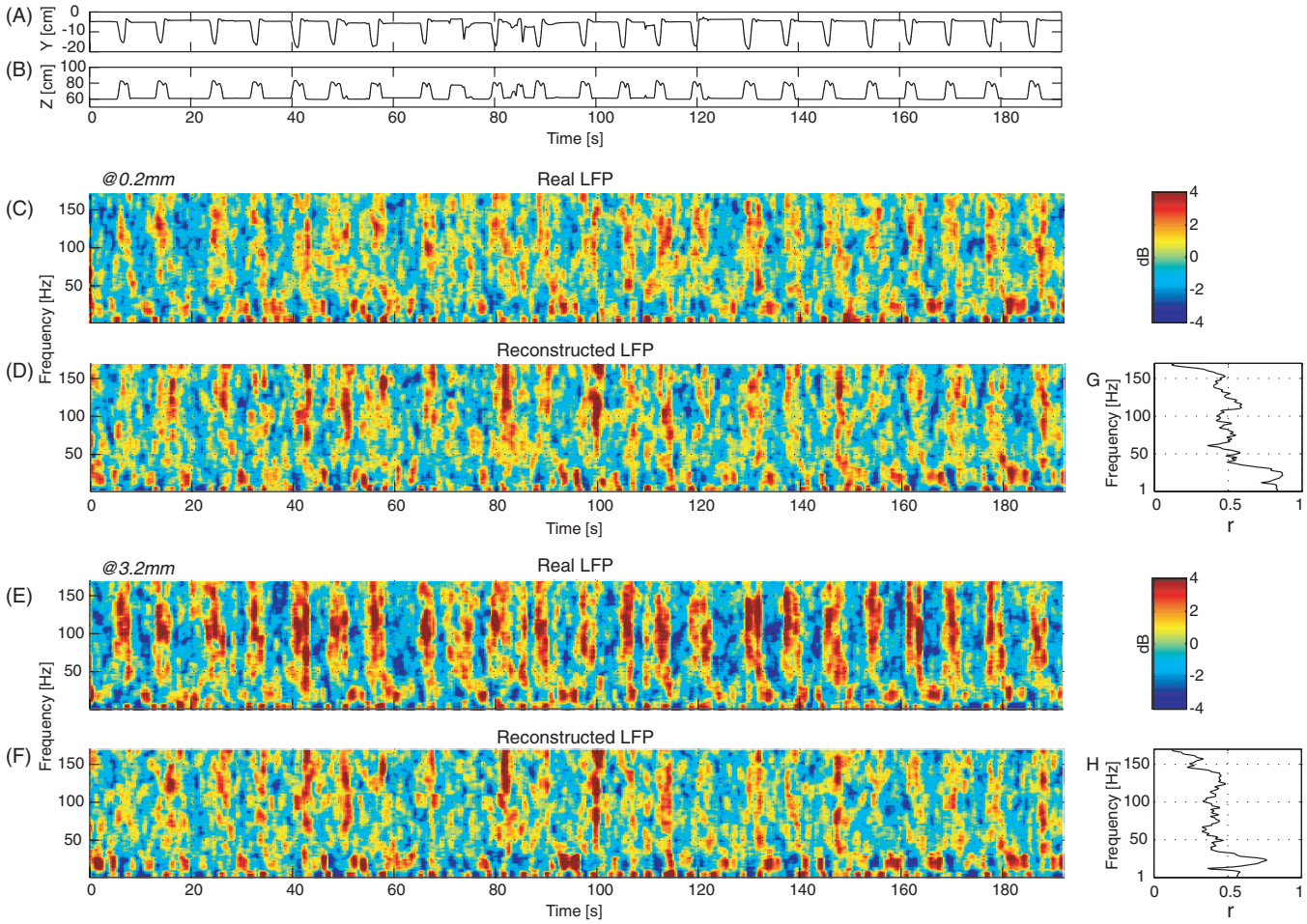

Figure 6. Time-frequency analysis of reconstructed LFP signals in novel sessions. (A and B) Hand trajectories along the Y (A) and Z (B) axes in an entire single session consisting of 23 trials. (C and E) Time-frequency analyses of real LFP signals at depths of 0.2 mm and 3.2 mm from the cortical surface, respectively. (D and F) Time-frequency analyses of reconstructed LFP signals at depths 0.2 mm and 3.2 mm, respectively. For the calculation of reconstructed LFPs, the weighted summation with the best correlation coefficient among the 23 trials was used. Correlation coefficients between the real LFP signal and reconstructed LFP signal at 0.2 mm and 3.2 mm were 0.71 and 0.50, respectively. The time-resolution was 3.3 Hz. (G and H) Correlation coefficients at each frequency. The resolution of the frequency range is 1 Hz. Note, the powers of 15–30 Hz and 110–140 Hz frequency signals of the reconstructed LFP alternated depending on the state of the arm-movement, as did those of the real LFP signal, even at 3.2 mm.

from brain surfaces, because the high-γ band component of the LFP reflects the spiking activity (Ray *et al* 2008). Although there is no correlation between ECoG and LFPs under 2 mm depth in these high-γ band signals, the frequency signals could be reconstructed with slight correlation by SLiR. Our reconstruction of the deep layer neuronal signal from the ECoG signals surely presents a novel way of less invasively estimating the output from the deeper cortical layers. Moreover, analysis of the weights for reconstruction of LFP reveal the spatiotemporal contribution of ECoG signals to reconstructions of LFPs according to their depths. Our results provide not only a new methodology to be used for less invasive BMIs, but also information offering insights into the relationship between LFP and ECoG signals.

Development of multi-channel electrode arrays from Parylene-C for ECoG recordings

Recently, multi-channel ECoG electrodes were introduced to record the neural activity from wide cortical areas (Rubehn *et al* 2009). Performance of the electrode array was studied relative to inter-electrode distances; the optimal inter-electrode spacing of subdual electrodes was 0.7 mm in awake rats and ∼1.7 mm in the human model (Slutzky *et al* 2010). Use of the same type of ECoG array that was customized for the current experiments has already been reported in rats (Toda *et al* 2011b), where its ability to decode visually evoked activity in the occipital cortex was examined. However, an appropriate algorithm to use the micro-ECoG array to estimate the intracortical activity needed to be developed. As a relatively simple experimental model system, we first tested the ECoG array in electrophysiological experiments to characterize its performance in detecting event-related signals in the barrel cortex of urethane-anesthetized rats (Sakatani *et al* unpublished observation). In the present study, we used a similar method to estimate intracortical activity in a more complex situation, the activity of M1 in an awake behaving monkey.

The thin, flexible structure of the ECoG array allowed us to detected motor-related cortical signals for six months after the surgery (data not shown). During the implantation surgery, we observed that the ECoG arrays were well fitted to the surface of the brain. The thin structure of the ECoG array (20 μm thick) also protected the brain parenchyma from excessive tension of the dura after the suture.

The high density ECoG electrode array required a small electrode-tip. Higher impedance electrodes measure signals originating from smaller areas around the tip of the electrode. For detecting signals with rich information from the ECoG, a higher impedance electrode is not suitable, and the platinum-black coating on the electrode-tip provided low electronic impedance. The platinum coating was made by evaporating the substrate of the ECoG electrode and made the array resistant to breaking during its implantation. The platinum coating was not broken up to six months after implantation surgery in the case of another test subject.

Sparse linear regression

We applied the sparse linear regression (SLiR) to simultaneously recorded, multichannel measures of neural activity from the brain. The SLiR enabled reconstructions of finger-movements, finger-forces and arm-EMG patterns from near-infrared spectroscopy signals (Nambu *et al* 2009), cortical current dipoles (Toda *et al* 2011a), blood oxygen level-dependent signals (Ganesh *et al* 2008) and neural firing (Ting *et al* 2008). The spiking activity of a population of neurons was modeled by LFPs/EEG in the monkey visual cortex using a general linear regression (Whittingstall *et al* 2009, and its supplemental figure 4). In this study, we used the SLiR for the first time to estimate intracortical LFPs from ECoG signals during arm movements of an awake behaving monkey and confirmed the accuracy of the estimations by comparing the time-frequency patterns of the reconstructed data with those of the real LFP data in the M1. Our results suggested that when information from multiple ECoG channels was combined, estimations of LFPs, even in deeper cortical layers, were much improved.

In this experiment, we used a time lag of 0–1 s to calculate the weighted summations. Our data showed that including the past information from the ECoG recordings as a 'spatiotemporal weighted summation' improved the accuracy of reconstruction compared to using the ECoG records of the same moment as a 'spatial weighting' for the broad band, the β band and the high-γ band components (figures 4(C)–(E)). The degree of improvement seemed to be larger for the deeper layer LFPs. This result indicates that the earlier ECoG records contain useful information for reconstructing the deeper layer LFPs, which suggests that activities in the superficial layers have a causal relationship to the future activities in the deeper layer. If the sensory feedback signals caused by movements generated by the activity of neurons in layer V are included in the signals recorded in the superficial layers of the M1, including subsequent signals (i.e. a time-*lag* to the future) might also contribute to improving the accuracy of reconstruction; however, we did not test this in this study, because the subsequent ECoG signal cannot be used in real-time control of a BMI. Linear regression approaches using a machine learning algorithm such as the SLiR do not necessarily reveal direct causality among neuronal signals in the physiological context. However, the current results indicated that including the earlier ECoG information improves the accuracy of reconstructing the subsequent LFP in the deeper layers, and such results are suggestive of neural representation in the brain. In addition, it was found in the present study that the distribution of ECoG channels that remained effective for reconstructing the LFP following the selection process of the SLiR, was dependent on their distance from the LFP probe. Reconstruction of deeper layer LFPs required ECoG signals from a wider extent compared to those for the more superficial LFPs (figure 5(G)). This tendency seems to reflect the property of signal propagation in the cortical tissue. Correlated activity along the apical dendrites of large pyramidal neurons induces a major dipole orientated perpendicularly to the cortical surface. The ECoG signal reflects the assembly of these dipoles generated over the area of several hundreds of micrometers in diameter under each ECoG electrode. However, it is not yet clear how the ECoG signal represents the intracortical neuronal activity and its propagation via synapses. The present findings showed that earlier information in the ECoG signals contributes to reconstruction of deeper layer LFPs (figure 5(J)), suggesting that the LFP signal involves not only physical propagation of electrical signals recorded by the ECoG, but also reflects signals generated through neuronal dynamics in the local circuits. Our obvious next step is to perform a current–source density analysis (Pitts 1952, Freeman and Nicholson 1975, Mitzdorf 1985) and partial coherence analysis (Kocsis *et al* 1999), both of which will surely give insight into the neuronal dynamics of cortical local circuits and behavioral outcome from the parameters estimated in this way. If we could properly perform these analyses based on the reconstructed LFPs, it is expected not only to enable us to accurate decoding of motor output from the motor cortex, but also to give us deeper insights into the relation between the dynamics of cell assembly and brain functions.

Frequency analysis of recorded neural activities and their application for BMI control

The present study demonstrated the possibility of reconstructing LFP components of various frequency ranges. It is well known that the δ band component reflects the period of deep sleep (e.g. Steriade 2006). Recently, δ-range activities were shown to be informative of input stimulus (Montemurro *et al* 2008), linked to attentional selection (Lakatos *et al* 2008), and related to arm-movements of monkeys (Bansal *et al* 2011) and humans (Ball *et al* 2009). From a view of studies about hand and finger movements (Zanos *et al* 2008, Pistohl *et al* 2012), low frequency components recoded from ECoG array would have important implications for preshaping during reach-and-grasping movements. Moreover, the neuronal signals in the δ-range were also useful for moving a cursor with a prosthetic device, using the chin in

humans (Saleh *et al* 2010). In the present study, the power of the low-frequency LFPs, such as the δ band component, increased remarkably both in the deeper layer LFP and the cortical surface ECoG recordings at the onset and offset of arm movements (figure 2(F)). The increase in the δ band component was observed at the movement onset, between the disappearance of the β band signal and the appearance of the high-γ band activity. In this paper we did not focus on the δ band signals (1–4 Hz). However, it actually increased around the movement initiation, approximately 1.5 s before the timing of reaching offset (figure 2(F)). Moreover, as shown in figure 6, the δ band signals were reconstructed with high accuracy (at 0.2 mm, $r_\delta = 0.82 \pm 0.005$; at 3.2 mm, $r_\delta = 0.57 \pm 0.007$ between reconstructed and real LFPs across all cross-validation trials). For future studies, detection of such an increase in the δ band signal may be useful for decoding the motor output from the ECoG signal.

The LFPs reconstructed in this experiment seem to carry information about individual phases of arm movements, such as rest, reach and hand-withdrawal, by detecting the shift in activation of various frequency components. These results suggest the possibility of estimating the kinematics of arm movements with high accuracy not only with ECoG signals but also with the 'estimated' LFP signals. To achieve high decoding accuracy by the algorithm based on the weighted summation of multichannel ECoG signals learned with previously acquired neuronal datasets from another subject is our future goal.

Acknowledgments

This study is the result of 'Brain Machine Interface Development' carried out under the Strategic Research Program for Brain Sciences by the Ministry of Education, Culture, Sports, Science and Technology of Japan. We thank M Togawa (NIPS) and Y Yamanishi (NIPS) for their assistance with our experiments. We are grateful to K Takahashi (University of Chicago) for helpful suggestions about the design, recording and analysis of the multiunit-recording system combined with the motion capture system in monkey. We also thank M Yoshida (NIPS) and T Sakatani (NIPS) for general support; H Toda (Niigata University), H Sawahata (Niigata University) and I Hasegawa (Niigata University) for technical collaborations; and O Yamashita (ATR), J Morimoto (ATR), K Toyama (Shimazu Co.), S Sakatani (RIKEN) and H Tamura (Osaka University) for their discussion.

References

Andersen R A, Hwang E J and Mulliken G H 2010 Cognitive neural prosthetics *Annu. Rev. Psychol.* **61** 169–90

Ball T, Schulze-Bonhage A, Aertsen A and Mehring C 2009 Differential representation of arm movement direction in relation to cortical anatomy and function *J. Neural. Eng.* **6** 016006

Bansal A K, Vargas-Irwin C E, Truccolo W and Donoghue J P 2011 Relationships among low-frequency local field potentials, spiking activity, and three-dimensional reach and grasp kinematics in primary motor and ventral premotor cortices *J. Neurophysiol.* **105** 1603–19

Chao Z C, Nagasaka Y and Fujii N 2010 Long-term asynchronous decoding of arm motion using electrocorticographic signals in monkeys *Front. Neuroeng.* **3** 3

Chase S M, Schwartz A B and Kass R E 2010 Latent inputs improve estimates of neural encoding in motor cortex *J. Neurosci.* **30** 13873–82

Crone N E, Miglioretti D L, Gordon B and Lesser R P 1998 Functional mapping of human sensorimotor cortex with electrocorticographic spectral analysis. II. Event-related synchronization in the gamma band *Brain* **121** 2301–15

Freeman J A and Nicholson C 1975 Experimental optimization of current source-density technique for anuran cerebellum *J. Neurophysiol.* **38** 369–82

Ganesh G, Burdet E, Haruno M and Kawato M 2008 Sparse linear regression for reconstructing muscle activity from human cortical fMRI *Neuroimage* **42** 1463–72

Georgopoulos A P, Kalaska J F, Caminiti R and Massey J T 1982 On the relations between the direction of two-dimensional arm movements and cell discharge in primate motor cortex *J. Neurosci.* **2** 1527–37

Hatsopoulos N G and Donoghue J P 2009 The science of neural interface systems *Annu. Rev. Neurosci.* **32** 249–66

Hochberg L R, Serruya M D, Friehs G M, Mukand J A, Saleh M, Caplan A H, Branner A, Chen D, Penn R D and Donoghue J P 2006 Neuronal ensemble control of prosthetic devices by a human with tetraplegia *Nature* **442** 164–71

Katzner S, Nauhaus I, Benucci A, Bonin V, Ringach D L and Carandini M 2009 Local origin of field potentials in visual cortex *Neuron* **6** 35–41

Kocsis B, Bragin A and Buzsáki G 1999 Interdependence of multiple theta generators in the hippocampus: a partial coherence analysis *J. Neurosci.* **19** 6200–12

Lakatos P, Karmos G, Mehta A D, Ulbert I and Schroeder C E 2008 Entrainment of neuronal oscillations as a mechanism of attentional selection *Science* **320** 110–13

Leuthardt E C, Schalk G, Wolpaw J R, Ojemann J G and Moran D W 2004 A brain-computer interface using electrocorticographic signals in humans *J. Neural Eng.* **1** 63–71

Lindén H, Tetzlaff T, Potjans T C, Pettersen K H, Grün S, Diesmann M and Einevoll G T 2011 Modeling the spatial reach of the LFP *Neuron* **72** 859–72

Marsden J F, Werhahn K J, Ashby P, Rothwell J, Noachtar S and Brown P 2000 Organization of cortical activities related to movement in humans *J. Neurosci.* **20** 2307–14

Mehring C, Nawrot M P, de Oliveira S C, Vaadia E, Schulze-Bonhage A, Aertsen A and Ball T 2004 Comparing information about arm movement direction in single channels of local and epicortical field potentials from monkey and human motor cortex *J. Physiol. Paris* **98** 498–506

Mehring C, Rickert J, Vaadia E, Cardosa de Oliveira S, Aertsen A and Rotter S 2003 Inference of hand movements from local field potentials in monkey motor cortex *Nat. Neurosci.* **6** 1253–4

Mitzdorf U 1985 Current source-density method and application in cat cerebral cortex: investigation of evoked potentials and EEG phenomena *Physiol. Rev.* **65** 37–100

Montemurro M A, Rasch M J, Murayama Y, Logothetis N K and Panzeri S 2008 Phase-of-firing coding of natural visual stimuli in primary visual cortex *Curr. Biol.* **18** 375–80

Moran D W and Schwartz A B 1999 Motor cortical representation of speed and direction during reaching *J. Neurophysiol.* **82** 2676–92

Nambu I, Osu R, Sato M A, Ando S, Kawato M and Naito E 2009 Single-trial reconstruction of finger-pinch forces from human motor-cortical activation measured by near-infrared spectroscopy (NIRS) *Neuroimage* **47** 628–37

Nicolelis M A and Lebedev M A 2009 Principles of neural ensemble physiology underlying the operation of brain-machine interfaces *Nat. Rev. Neurosci.* **10** 530–40

Ohara S *et al* 2001 Increased synchronization of cortical oscillatory activities between human supplementary motor and primary sensorimotor areas during voluntary movements *J. Neurosci.* **21** 9377–86

Pesaran B, Pezaris J S, Sahani M, Mitra P P and Andersen R A 2002 Temporal structure in neuronal activity during working memory in macaque parietal cortex *Nat. Neurosci.* **5** 805–11

Pistohl T, Schulze-Bonhage A, Aertsen A, Mehring C and Ball T 2012 Decoding natural grasp types from human ECoG *Neuroimage* **59** 248–60

Pitts W 1952 Investigation of synaptic transmission *Cybernetics. Trans. 9th Conf. Josiah Macy Foundation (New York)* ed Von Foerster pp 159–62

Ray S, Crone N E, Niebur E, Franaszczuk P J and Hsiao S S 2008 Neural correlates of high-gamma oscillations (60–200 Hz) in macaque local field potentials and their potential implications in electrocorticography *J. Neurosci.* **28** 11526–36

Rickert J, Oliveira S C, Vaadia E, Aertsen A, Rotter S and Mehring C 2005 Encoding of movement direction in different frequency ranges of motor cortical local field potentials *J. Neurosci.* **25** 8815–24

Rubehn B, Bosman C, Oostenveld R, Fries P and Stieglitz T 2009 A MEMS-based flexible multichannel ECoG-electrode array *J. Neural. Eng.* **6** 036003

Saleh M, Reimer J, Penn R, Ojakangas C L and Hatsopoulos N G 2010 Fast and slow oscillations in human primary motor cortex predict oncoming behaviorally relevant cues *Neuron* **65** 461–71

Scherberger H, Jarvis M R and Andersen R A 2005 Cortical local field potential encodes movement intentions in the posterior parietal cortex *Neuron* **46** 347–54

Schwartz A B, Cui X T, Weber D J and Moran D W 2006 Brain-controlled interfaces: movement restoration with neural prosthetics *Neuron* **52** 205–20

Slutzky M W, Jordan L R, Krieg T, Chen M, Mogul D J and Miller L E 2010 Optimal spacing of surface electrode arrays for brain-machine interface applications *J. Neural. Eng.* **7** 026004

Steriade M 2006 Grouping of brain rhythms in corticothalamic systems *Neuroscience* **137** 1087–106

Ting J A *et al* 2008 Variational Bayesian least squares: an application to brain-machine interface data *Neural Netw.* **21** 1112–31

Toda A, Imamizu H, Kawato M and Sato M A 2011a Reconstruction of two-dimensional movement trajectories from selected magnetoencephalography cortical currents by combined sparse Bayesian methods *Neuroimage* **54** 892–905

Toda H, Suzuki T, Sawahata H, Majima K, Kamitani Y and Hasegawa I 2011b Simultaneous recording of ECoG and intracortical neuronal activity using a flexible multichannel electrode-mesh in visual cortex *Neuroimage* **54** 203–12

Velliste M, Perel S, Spalding M C, Whitford A S and Schwartz A B 2008 Cortical control of a prosthetic arm for self-feeding *Nature* **453** 1098–101

Whittingstall K and Logothetis N K 2009 Frequency-band coupling in surface EEG reflects spiking activity in monkey visual cortex *Neuron* **64** 281–9

Wolpaw J R 2007 Brain-computer interfaces as new brain output pathways *J. Physiol.* **579** 613–9

Yanagisawa T, Hirata M, Saitoh Y, Kishima H, Matsushita K, Goto T, Fukuma R, Yokoi H, Kamitani Y and Yoshimine T 2012 Electrocorticographic control of a prosthetic arm in paralyzed patients *Ann. Neurol.* **71** 353–61

Zanos S, Miller K J and Ojemann J G 2008 Electrocorticographic spectral changes associated with ipsilateral individual finger and whole hand movement *Conf. Proc. IEEE Eng. Med. Biol. Soc.* **2008** 5939–42